Pushing point-spread function reconstruction to the next level

Beltramo-Martin, O.; Marasco, A.; Fusco, T.; Massari, D.; Milli, J.; Fiorentino, G.; Neichel, B.

Published in:
Monthly Notices of the Royal Astronomical Society

DOI:
10.1093/mnras/staa525

Monthly Notices
of the
ROYAL ASTRONOMICAL SOCIETY

MNRAS **494,** 775–788 (2020) doi:10.1093/mnras/staa525

Pushing point-spread function reconstruction to the next level: application to SPHERE/ZIMPOL

O. Beltramo-Martin [1,2]★ A. Marasco [3,4] T. Fusco,[1,2] D. Massari [3,4,5] J. Milli,[6,7] G. Fiorentino [8] and B. Neichel[2]

[1]*ONERA, The French Aerospace Laboratory, BP 72, F-92322 Chatillon Cedex, France*
[2]*Aix Marseille Univ., CNRS, CNES LAM, 38 rue F. Joliot-Curie, 13388 Marseille, France*
[3]*INAF – Osservatorio di Astrofisica e Scienza dello Spazio di Bologna, Via Gobetti 93/3, I-40129 Bologna, Italy*
[4]*Kapteyn Astronomical Institute, University of Groningen, NL-9747 AD Groningen, the Netherlands*
[5]*Dipartimento di Fisica e Astronomia, Università degli Studi di Bologna, Via Gobetti 93/2, I-40129 Bologna, Italy*
[6]*European Southern Observatory (ESO), Alonso de Córdova 3107, Vitacura, Casilla 19001, Santiago, Chile*
[7]*Univ. Grenoble Alpes, CNRS, IPAG, F-38000 Grenoble, France*
[8]*INAF – Osservatorio Astronomico di Roma, via Frascati 33, 0040 Monte Porzio Catone, Italy*

Accepted 2020 February 18. Received 2020 January 28; in original form 2019 September 18

ABSTRACT

Point-spread function (PSF) reconstruction (PSF-R) is a well-established technique to determine the PSF reliably and accurately from adaptive optics (AO) control-loop data. We have successfully applied this technique to improve the precision of photometry and astrometry for observations of NGC 6121 obtained with the Spectro Polarimetric High-contrast Exoplanet REsearch (SPHERE)/Zurich IMaging POLarimeter (ZIMPOL), which will be presented in a forthcoming Letter. First, we present the methodology we followed to reconstruct the PSF by combining pupil-plane and focal-plane measurements using our PSF-R method PRIME (PSF Reconstruction and Identification for Multiple-source characterization Enhancement), with upgrades of both the model and best-fitting steps compared with previous articles. Secondly, we highlight that PRIME allows us to maintain the PSF fitting residual below 0.2 per cent over 2 hours of observation and using only 30 s of AO telemetry, which may have important consequences for telemetry storage for PSF-R purposes on future 30–40 m class telescopes. Finally, we deploy PRIME in a more realistic regime using faint stars, so as to identify the precision needed on the initial-guess parameters to ensure convergence towards the optimal solution.

Key words: atmospheric effects – instrumentation: adaptive optics – methods: analytical – methods: data analysis.

1 INTRODUCTION

Point-spread function (PSF) analysis of seeing and diffraction-limited images in crowded stellar fields has been a consolidated technique since the late 1980s. There are several commonly used astronomical packages that apply this technique successfully, such as STARFINDER (Diolaiti et al. 2000), SEXTRACTOR (Bertin & Arnouts 1996) or DAOPHOT (Stetson 1987). These are essentially based on extraction and modelling of the PSF using isolated stars across the scientific field of view (FoV). This task can be particularly challenging in two opposite cases: in very dense stellar fields, like the core of globular clusters, where solid PSF modelling is compromised by confusion, and in sparsely dense fields surrounding isolated galaxies, where no or few point-like sources are available for PSF modelling. These two situations become even more demanding when observing with adaptive optics (AO) instruments, since the size of the imaged FoV ranges typically from tens of arcsec to a few arcmin, thus preventing us very often from having isolated stars at our disposal for a robust PSF analysis. Furthermore, when dealing with AO systems, the complexity of the PSF increases compared with seeing-limited images and, last but not least, real-time turbulence correction makes the PSF change across the FoV, the time and the spectrum. The combination of source crowding and PSF inhomogeneity affects the estimate of source parameters like magnitude and position strongly (Schödel 2010; Yelda et al. 2010; Massari et al. 2016a,b). Photometric and astrometric accuracy can be enhanced using innovative approaches that account for AO PSF spatial variation models (Ciurlo et al. 2018; Witzel et al. 2016).

In the new era of giant segmented mirror telescopes (GSMTs), fed mainly by AO modules, our ability to perform good PSF fitting will be crucial. In fact, we aim to improve the photometric and

★ E-mail: olivier.beltramo-martin@lam.fr

astrometric accuracy and precision by at least a factor of three, while the complexity of the PSF structure will increase. In this context, an alternative PSF determination approach, so-called PSF reconstruction (PSF-R), has been investigated for 20 years. This method uses information from AO control-loop data in order to build a theoretical PSF model, as summarized in Section 2. As analysed in Ascenso et al. (2015), PSF-R is truly promising to tackle the actual limitations of standard standalone image processing pipelines. However, PSF-R has never reached the point of being fully integrated into dedicated software for image analysis and being operable for astronomers, who are calling for PSF-R to be pushed to a more suitable mode for later implementation in a pipeline.

Moreover, one of the major issues PSF-R developers experience is the calibration of scalar system parameters, such as seeing and wavefront sensor (WFS) optical gains, for instance. Although it remains feasible to identify these parameters from the telemetry, estimates are usually provided with 10 per cent accuracy (Jolissaint et al. 2018), which limits the PSF-R accuracy to close to the same percentage, as we illustrate in Section 2.3. Another way to state this is that handling the sole AO telemetry alone is not sufficient to reach 1 per cent level accuracy in the PSF. However, very accurate PSF estimates at 1 per cent level may be needed, especially for stellar population analysis. In this context, we have introduced PRIME (Beltramo-Martin et al. 2019) as a novel approach that combines pupil-plane (AO telemetry) and focal-plane (imager frames) data to overcome the problem of system parameter identification and therefore optimize the PSF-R.

We have successfully deployed PRIME on NGC 6121 images obtained in 2018 with the Zurich IMaging POLarimeter (ZIMPOL) instrument (Schmid et al. 2018) mounted at the focal plane of the Spectro Polarimetric High-contrast Exoplanet REsearch (SPHERE) instrument (Beuzit et al. 2019) on the Very Large Telescope (VLT). The results showed a factor of 10 improvement in photometric precision and will be presented in an upcoming article (Massari et al. 2020). First, we are willing in this article to present the exact methodology we followed to reconstruct the PSF using an upgraded version of PRIME presented in Section 3.1. Secondly, another major drawback of PSF-R for future GSMTs lies in the large amount of telemetry data we must handle and archive for every observation. With PRIME, we show in Section 3.2 that we can mix 30 s of telemetry data with images acquired 2 h later and still achieve an accurate PSF determination below 0.2 per cent of the mean residual, which offers the possibility not to store the full AO telemetry during observation. Finally, in Section 4, we present a utilization of PRIME in a more realistic scenario using faint stars ($m_V = 15$–16 mag) and compare the reconstructed PSF with the on-axis bright source ($m_V = 10.6$ mag) of the NGC 6121 field. In order to mitigate noise propagation into the criterion-solving, we compare different methods to constrain the solution using either hard bounds or a Gaussian statistics assumption on parameters and draw conclusions regarding the best strategy. Discussions and conclusions are given in Section 5.

2 RECONSTRUCTING THE PSF

PSF-R derives from the image formation theory proposed by Roddier (1981) to connect the focal-plane image to the incoming wavefront distortions within the pupil plane. In the case in which we neglect scintillation effects and assume that the phase of the electric field in the pupil plane is spatially stationary, the long-exposure (e.g. the acquisition time is much larger than the turbulence coherence time) optical transfer function (OTF), defined as the PSF Fourier transform, is decomposed as the following multiplication:

$$\tilde{h}(\boldsymbol{\rho}/\lambda) = \tilde{h}_{\mathrm{T}}(\boldsymbol{\rho}/\lambda) \cdot \tilde{h}_{\varepsilon}(\boldsymbol{\rho}/\lambda), \tag{1}$$

where $\boldsymbol{\rho}/\lambda$ is the angular frequency with λ the observation wavelength, $\tilde{h}$ the total OTF, $\tilde{h}_{\mathrm{T}}$ the telescope + instrument OTF that is derived from the pupil function autocorrelation and $\tilde{h}_{\varepsilon}$ the residual atmospheric OTF. PSF-R aims at estimating $\tilde{h}_{\varepsilon}$ from

$$\tilde{h}_{\varepsilon}(\boldsymbol{\rho}/\lambda) = \exp\left[\mathcal{B}_{\varepsilon}(\boldsymbol{\rho}) - \mathcal{B}_{\varepsilon}(0)\right], \tag{2}$$

where $\mathcal{B}_{\varepsilon}$ is the residual phase covariance function, which can theoretically be captured from the AO control-loop data, i.e. the WFS measurements and commands applied to the deformable mirror (DM). $\mathcal{B}_{\varepsilon}$ is split into a sum of covariance error terms, assumed to be independent of each other, as follows:

$$\mathcal{B}_{\varepsilon}(\boldsymbol{\rho}) = \mathcal{B}_{\perp}(\boldsymbol{\rho}) + \mathcal{B}_{\parallel}(\boldsymbol{\rho}) + \mathcal{B}_{\Delta}(\boldsymbol{\rho}), \tag{3}$$

where $\mathcal{B}_{\perp}$ refers to uncompensated spatial frequencies, while $\mathcal{B}_{\parallel}$ includes the AO residual only and $\mathcal{B}_{\Delta}$ corresponds to the anisoplanatism effect. The calculation of this latter can be found in multiple references (Whiteley, Welsh & Roggemann 1998; Fusco et al. 2000; Flicker, Rigaut & Ellerbroek 2003; Britton 2006; Beltramo-Martin et al. 2018). In the case of SPHERE/ZIMPOL, we only need to account for angular anisoplanatism that is produced by the spatial decorrelation of the incoming wavefront. In the V band, the typical isoplanatic angle at Paranal has been measured as $\theta_0 = 2$ arcsec (Osborn et al. 2018; Masciadri, Lombardi & Lascaux 2014), which is the separation from the guide star beyond which the PSF becomes significantly elongated by the anisoplanatism effect.

2.1 Reconstruction of uncompensated modes

$B_{\perp}(\boldsymbol{\rho})$ is calculated from the perpendicular power spectrum density (PSD) as follows:

$$\mathcal{B}_{\perp}(\boldsymbol{\rho}) = \mathcal{F}^{-1}[\mathcal{W}_{\perp}(\boldsymbol{k}/\lambda)], \tag{4}$$

where $\mathcal{F}^{-1}$ is the Fourier operator and $\mathcal{W}_{\perp}$ is the Von Kármán atmospheric PSD filtered by the corrected frequencies:

$$\mathcal{W}_{\perp}(\boldsymbol{k}) = \begin{cases} 0.0229 r_0^{-5/3} \left(k^2 + 1/L_0^2\right)^{-11/6} & \text{if } k > k_{\mathrm{AO}}, \\ 0 & \text{otherwise}, \end{cases} \tag{5}$$

where r_0 is Fried's parameter (connected to the seeing), $k = |\boldsymbol{k}|$ and k_{AO} is the AO cut-off frequency approximated by $k_{\mathrm{AO}} \simeq n_{\mathrm{act}}/2D$, where n_{act} is the number of actuators per row and D the pupil diameter. This cut-off frequency is a function of the number of controlled modes, but we can still define an equivalent value of n_{act} that produces the same fitting error, in the sense that this approximation is not critical for the following. The fitting PSD can be calculated once and scaled regarding the r_0 value.

2.2 Reconstruction of corrected modes

$\mathcal{B}_{\parallel}$ is computed directly from the AO telemetry (Veran et al. 1997). However, some care must be given to the aliasing, which affects WFS measurements and PSF morphology. In the case of a large bandwidth system (with a measurement rate of 1380 Hz, SPHERE complies with this hypothesis), Veran et al. (1997) shows that the phase produced by the DM is anticorrelated with the WFS aliasing perturbation created by high-order modes. Therefore, calculations show that, to account for aliasing in the PSF-R process, one must add the aliasing closed-loop covariance to the covariance function

derived from WFS slopes (that is, contaminated by the aliasing). Moreover, tip–tilt modes are corrected using a linear quadratic Gaussian (LQG) algorithm (Petit et al. 2014), while higher order modes are controlled using a modal optimization-based integrator (Petit et al. 2008). This does not matter in the present case, expect for noise-variance modelling for faint guide stars; however, we will have to handle tip–tilt modes differently from other corrected ones in Section 3 and we introduce herein a split reconstruction for later use. Eventually, we have

$$\mathcal{B}_{\parallel}(\boldsymbol{\rho}) = \mathcal{B}_{\rm AO}(\boldsymbol{\rho}) + \mathcal{B}_{\rm TT}(\boldsymbol{\rho}) + \mathcal{B}_{\rm AL}(\boldsymbol{\rho}), \tag{6}$$

where $\mathcal{B}_{\rm AO}$ is the tip–tilt excluded AO residual phase covariance, $\mathcal{B}_{\rm TT}$ the residual jitter covariance and $\mathcal{B}_{\rm AL}$ the model of the aliasing covariance that affects the PSF.

2.2.1 Reconstruction of tip–tilt excluded modes

The methodology for calculating $\mathcal{B}_{\rm AO}$ from WFS measurements is highly spread in the literature (Veran et al. 1997; Gilles et al. 2012; Jolissaint, Ragland & Wizinowich 2015; Ragland et al. 2018; Beltramo-Martin et al. 2019); in practice, we used the Vii algorithm proposed by Gendron et al. (2006), where

$$\mathcal{B}_{\rm AO}(\boldsymbol{\rho}) = \sum_{i}^{n_{\rm act}} \Lambda(i,i) V_{ii}(\boldsymbol{\rho}), \tag{7}$$

where V_{ii} are the Vii functions obtained from the eigendecomposition of the matrix of high-order deformable mirror (HODM) influence functions (HODM influence matrix). The use of the Vii functions allows us to speed up the covariance calculation significantly. Λ is the diagonal matrix that contains the eigenvalues of the covariance matrix $\mathcal{C}_{\rm AO}$. This latter is estimated empirically from the tip–tilt excluded WFS measurements as follows (Vigan et al. 2019):

$$\mathcal{C}_{\rm AO} = \left(\frac{2\pi}{\lambda}\right)^2 \mathcal{R}_{\rm AO}(\langle \boldsymbol{s}.\boldsymbol{s}^t\rangle - \langle \boldsymbol{\eta}.\boldsymbol{\eta}^t\rangle)\mathcal{R}_{\rm AO}^t, \tag{8}$$

where $\mathcal{R}_{\rm AO}$ is the matrix that reconstructs the pointwise wavefront from the WFS measurements $\boldsymbol{s}$ that are contaminated by additive noise $\boldsymbol{\eta}$ and where $\langle \boldsymbol{x}.\boldsymbol{x}^t\rangle$ refers to the empirical covariance matrix of vector $\boldsymbol{x}$. The noise covariance can be estimated using an analytical formula (Rousset, Primot & Fontanella 1987), from the temporal autocorrelation of the measurements (Gendron & Léna 1995) or from their temporal PSD (Jolissaint et al. 2015), to mention only a few approaches. In the specific case of SPHERE/ZIMPOL, the reconstructor $\mathcal{R}_{\rm AO}$ is derived from successive multiplications of calibrated matrices:

$$\mathcal{R}_{\rm AO} = \left(\frac{632\times10^{-9}}{2\pi}\right) {\rm iF}.\boldsymbol{P}_{\rm M2V}.\boldsymbol{P}_{\rm S2M}.\boldsymbol{P}_{\rm AO}, \tag{9}$$

where

(i) iF is the calibrated HODM influence matrix that converts HODM voltages to a wavefront at 632 nm. It has a dimension of $240^2 \times n_{\rm act}$, where 240 is the pupil resolution in pixels during the calibration, which is interpolated to $2 \times n_{\rm act} + 1$ to speed up the reconstruction;

(ii) $\boldsymbol{P}_{\rm M2V}$ is the mode-to-voltage matrix that transforms $n_{\rm mode}$ Karhunen–Loève (KL) modes to $n_{\rm act}$ HODM voltages in stroke units;

(iii) $\boldsymbol{P}_{\rm S2M}$ is the slope-to-mode matrix that projects $2 \times n_{\rm subap}$ slope measurements in pixels to $n_{\rm mode}$ KL modes;

(iv) $\boldsymbol{P}_{\rm AO}$ is a $2n_{\rm subap} \times 2n_{\rm subap}$ matrix that filters the tip–tilt modes out from the slope measurements.

2.2.2 Reconstruction of tip–tilt modes

The tip–tilt covariance function in equation (3) is derived as follows:

$$\mathcal{B}_{\rm TT}(\boldsymbol{\rho}) = \frac{1}{D^2}\big(\mathcal{C}_{\rm TT}(1,1).\rho_x^2 + \mathcal{C}_{\rm TT}(2,2)\rho_y^2 + 2\times\mathcal{C}_{\rm TT}(1,2)\rho_x\rho_y\big), \tag{10}$$

where ρ_x, ρ_y are the x/y projection of the separation vector ρ from $-D/2$ to $\Omega/2$ and $\mathcal{C}_{\rm TT}$ is the tip–tilt covariance matrix,

$$\mathcal{C}_{\rm TT} = \left(\frac{2\pi}{\lambda}\right)^2 \mathcal{R}_{\rm TT}(\langle \boldsymbol{s}.\boldsymbol{s}^t\rangle - \langle \boldsymbol{\eta}.\boldsymbol{\eta}^t\rangle)\mathcal{R}_{\rm TT}^t, \tag{11}$$

where $\mathcal{R}_{\rm TT}$ permits us to reconstruct the tip–tilt wavefront over the pupil in metres using

$$\mathcal{R}_{\rm TT} = \frac{2.6\times\pi\times D}{180\times3600}.(\boldsymbol{P}_{\rm TT}.\boldsymbol{D}_{\rm V2S})^{\dagger}.\boldsymbol{P}_{\rm TT}, \tag{12}$$

with $(x)^{\dagger}$ the generalized invert matrix and where

(i) $\boldsymbol{P}_{\rm TT}$ is a $2 \times 2n_{\rm subap}$ matrix that projects the slope measurements on to tip–tilt modes and

(ii) $\boldsymbol{D}_{\rm V2S}$ is the $2\omega_{\rm subap} \times 2$ calibrated tip–tilt interaction matrix that converts the two tip–tilt DM commands into WFS slopes.

2.2.3 Reconstruction of the aliasing

The aliasing covariance function is derived from a model of the aliasing PSD $\mathcal{W}_{\rm AL}$ (Flicker 2008; Jolissaint 2010; Correia & Teixeira 2014) that accounts for the spatial filtering of the Shack–Hartmann WFS and the temporal propagation of the aliased measurement through the AO loop. Eventually we have

$$\mathcal{B}_{\rm AL}(\rho) = \mathcal{F}^{-1}[\mathcal{W}_{\rm AL}(\boldsymbol{k})], \tag{13}$$

with $\mathcal{W}_{\rm AL}$ calculated for any considered atmospheric layer by first aliasing the Von Kármán atmospheric PSD around a multiple of $1/d$, with d the sub-aperture size, and secondly propagating the PSD through the Shack–Hartmann spatial filter (Rigaut, Véran & Lai 1998) and the temporal rejection function of the loop, which is spatialized by replacing temporal frequencies with $\boldsymbol{f} = \boldsymbol{k}.\boldsymbol{v}_l$, where $\boldsymbol{v}_l$ is the velocity vector (norm is the windspeed value, angle is the wind direction) of the lth layer. We obtain the following expression for the aliasing PSD in closed-loop operation:

$$\mathcal{W}_{\rm AL}(\boldsymbol{k}) = \frac{0.0229 r_0^{-5/3}}{4{\rm sinc}(\boldsymbol{k}d)} \times \sum_{\substack{p=-\zeta\\ p\neq0}}^{\zeta}\sum_{\substack{q=-\zeta\\ q\neq0}}^{\zeta}\sum_{l=1}^{n_{\rm L}} \times f_l \frac{(\boldsymbol{k}^{-1}.\boldsymbol{k}_{pq})^2 {\rm sinc}(k_p d){\rm sinc}(k_q d)}{(k^2 + 1/L_0(l)^2)^{11/6}}.\mathcal{H}_{\rm cl}(l), \tag{14}$$

with

$$\mathcal{H}_{\rm cl}(l) = \frac{g^2{\rm sinc}(k_p v_{lx} t_i){\rm sinc}(k_q v_{ly} t_i)\exp(2{\rm i}\pi(k_p v_{lx} + k_q v_{ly})t_d)}{1 - 2(\iota - g)\cos(2\pi k_p v_{lx} t_i)\cos(2\pi k_q v_{ly} t_i) + (\iota - g)^2}, \tag{15}$$

where the following holds.

(i) $\boldsymbol{k}_{pq} = (k_p, k_q)$, with $k_p = k_x - p/d$ and $k_q = k_y - q/d$ as the x/y frequency vectors shifted by p/d and q/d, respectively.

(ii) ζ is a unitless number defined by the highest frequency seen by the WFS normalized by the DM cut-off frequency $k_{\rm AO}$. This number accounts for the spatial filtering in the WFS optical path that has been implemented to mitigate the aliasing effect as much as possible (Poyneer et al. 2006).

(iii) $v_{lx} = v_l \cos(\omega_l)$ and $v_{ly} = v_l \sin(\omega_l)$ are the components of the velocity vector at height h_l, projected respectively onto the x-axis and y-axis of the frequency plan, with v_l, ω_l the corresponding turbulence velocity and wind direction values at height h_l.

(iv) $L_0(l)$ is the outer scale vertical profile. In practice, we have chosen a flat profile and $L_0 = 25$, but methods exist to retrieve the integrated outer scale value from the telemetry (Andrade et al. 2019).

(v) t_i and t_d are respectively the WFS temporal sampling frequency and the loop delay, which is 2.3 frames (Cantalloube et al., in preparation).

(vi) g is the average of the modal gain vector (Petit et al. 2008). To be more accurate, we should evaluate how the WFS aliasing propagates through each controlled KL mode and though the AO loop by taking the modal optimization into account. However, such a description would increase the complexity of the aliasing PSD computation drastically for a small eventual improvement .

(vii) ι is the integrator leak factor, set to 1 (no leak) in the rest of this article.

2.3 Application to SPHERE/ZIMPOL

2.3.1 Data

We have acquired observations of NGC 6121 with the ZIMPOL V filter (central wavelength 554 nm, width 80.6 nm) in the context of technical calibrations[1] granted after the 2017 ESO calibration workshop.[2]

With a pixel scale of 7.2 mas pixel^{-1}, the detector covered a 3.5 arcsec × 3.5 arcsec field of view, as illustrated in Fig. 1. We summarize the acquisition time in Table 1 as well as the corresponding airmass value. The AO system ran at 300 Hz, instead of the nominal 1380 Hz, owing to the faintness ($V = 10.6$ mag) of the AO guide star and the grey dichroic used to share visible light between ZIMPOL and WFS. The data were acquired in field stabilization with the slow polarimetry readout mode, which provides readout noise seven times smaller that the standard imaging mode, to enhance the signal-to-noise ratio (S/N) of the fainter off-axis sources. The data were reduced using the SPHERE Data and Reduction Handling pipeline (DRH) to extract the intensity image, subtract a bias frame and correct for flat-field. Dedicated PYTHON routines were later used to recentre the individual frames, correct for bad pixels and average the frames in a single reduced image, as shown in Fig. 1.

The imaged field belongs to the central region of the aforementioned globular cluster and includes five stars, the brightest of which was used to guide the AO system. The four others are more than 1.7 arcsec away from the guide star. This field has been selected in order to quantify achievable limits on photometry and astrometry estimates of faint stars confused in the guide star halo; accurate *HST* measurements exist for comparison purposes.

On top of that, we had synchronous atmospheric parameters measurements delivered by, on the one hand, MASS-DIMM at Paranal (Butterley et al. 2018; Tokovinin & Kornilov 2007) as well as the stereo SCIDAR (Osborn et al. 2018) and, on the other hand, the AO real-time computer SPARTA (Fedrigo et al. 2006). We present the temporal evolution during the observation in Fig. 2. As already noticed by Milli et al. (2017), there are large discrepancies between SPARTA and MASS-DIMM estimates, but both claim that observing conditions were quite stable over the two observing slots. According to SPARTA, seeing and turbulence coherence time median values reached 0.6 arcsec and 11 ms respectively during the first part of the night, evolving to 0.5 arcsec and 9 ms during the second slot.

Finally, we have also two 30-s long data sets of AO control-loop data (WFS slopes, DM commands, calibrated matrices) obtained at 05h04m and 06h44m simultaneously with the beginning of ZIMPOL observations, as reported in Table 1. From the image, we have estimated a Strehl ratio (SR) in the V band from the

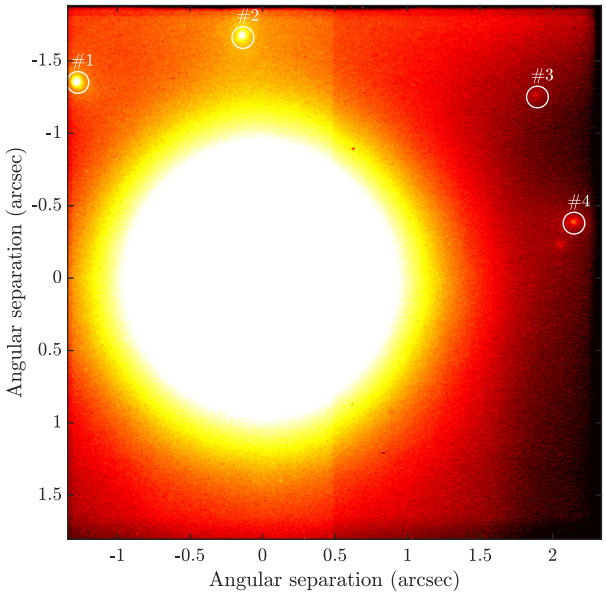

Figure 1. Stack of 26 frames of NGC 6121 observations obtained with SPHERE/ZIMPOL on 2018 June 26. Coordinates correspond to the distance in arcsec from the bright AO guide star. The field was 3.5 arcsec × 3.5 arcsec large and four off-axis stars, encircled in white and numbered, were imaged.

Table 1. Summary of NGC 6121 data acquired successively with ZIMPOL on the night of 2018 June 26, with a total of 26 images of 200 s exposure (NDIT=2, DIT = 100 s) each.

Acquisition date	Airmass	Acquisition date	Airmass
First slot of observations			
05:03:57 + **AO data**	1.169	05:26:06	1.238
05:07:17	1.18	05:29:26	1.243
05:11:27	1.191	05:33:23	1.265
05:14:47	1.201	05:36:43	1.282
05:18:49	1.213	05:42:11	1.300
05:22:09	1.225	05:45:31	1.315
Second slot of observations			
06:43:43 + **AO data**	1.672	07:08:57	1.934
06:47:03	1.704	07:12:55	1.977
06:51:00	1.737	07:16:15	2.177
06:54:20	1.771	07:20:19	2.077
06:58:18	1.809	07:23:39	2.118
07:01:38	1.849	07:27:36	2.186
07:05:37	1.889	07:30:56	2.271

[1]ESO program ID of observations: 60.A-9801(S)
[2]http://www.eso.org/sci/meetings/2017/calibration2017

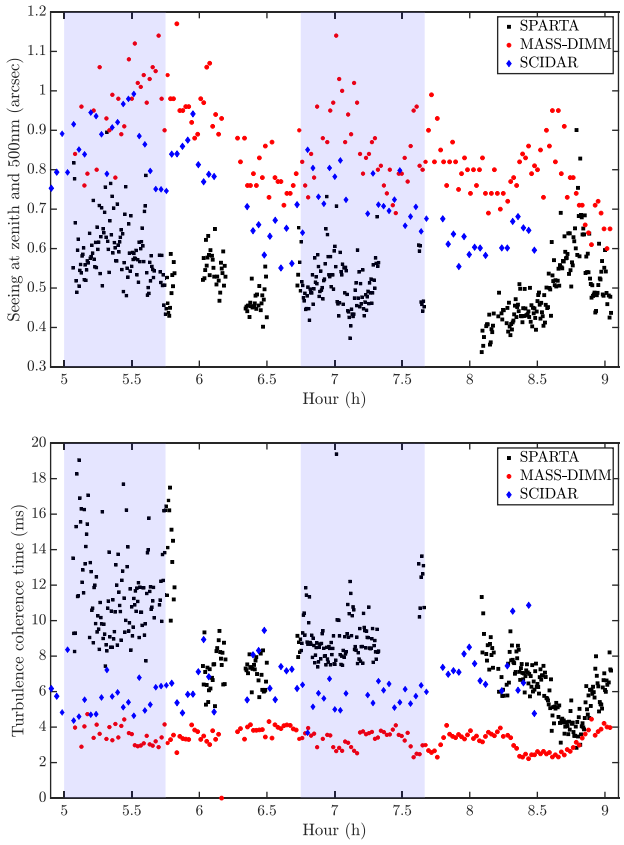

Figure 2. *Top:* seeing estimation at zenith and 500 nm. *Bottom:* turbulence coherence time estimation with respect to observing hour. Blue areas indicate the time window during which we had acquired ZIMPOL data.

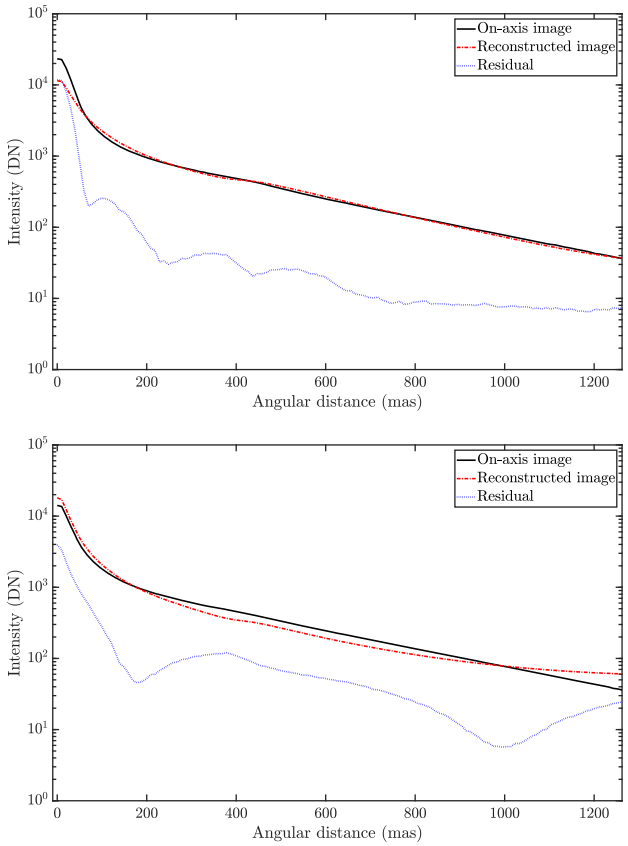

Figure 3. Azimuthal average of sky and reconstructed PSFs obtained with (top) 05:04 and (bottom) 06:43 data. The PSF was reconstructed using the same formalism presented in Section 2.

integration of the OTF over angular frequencies normalized to the diffraction-limit OTF. We obtained 1.4 ± 0.63 per cent over the whole observation, which corresponds to 182 nm ± 10, with a drop of 40 per cent in performance between slot 2 and slot 1.

2.3.2 *On-axis PSF-R results*

We have followed the mathematical formalism presented in Section 2 to reconstruct the PSF from the two AO data sets acquired at the beginning of each observing time slot. The methodology to treat the AO control-loop data was strictly the same, and we present in Fig. 3 reconstruction results compared with the on-axis image. To obtain a proper comparison, we have adjusted the photometry and astrometry by using a weighted best-fitting to scale the PSF over the on-axis image. Results are somehow disappointing for several reasons. First of all, PSF wings are not correctly retrieved systematically, as we see with the second case, for which r_0 is underestimated, i.e. the atmospheric disturbances are expected to be stronger than they actually were. Moreover, the reconstruction of the PSF core does not behave similarly, although the data processing is kept identical. We may have overestimation as well as underestimation of the PSF peak intensity.

This situation occurs systematically when trying PSF-R: current algorithms usually fail in achieving a stable, efficient and reproducible reconstruction across the multiple data sets they are tested on. There is a necessary need to calibrate the algorithm *a posteriori* over a subsample of data to approach the ultimate algorithm that would provide the same level of relative accuracy whatever the observing conditions. This calibration generally consists of applying some fudge factors to the telemetry (Clénet et al. 2008; Martin et al. 2016; Ragland et al. 2016) or/and to the noise variance. The main conclusion of more than 20 years of effort carrying out PSF-R is that PSF-R is not going to achieve proper PSF estimation by using the standard PSF-R framework.

2.3.3 *Off-axis PSF-R results using SCIDAR data*

As illustrated in Fig. 1, the field also contains off-axis stars that are sufficiently distanced from the guide star to potentially be contaminated by the anisoplanatism effect. We have access to stereo SCIDAR data at Paranal (Osborn et al. 2018) acquired during the same time slot as the ZIMPOL images. We report in Fig. 4 the $C_n^2(h)$ evolution across time and the corresponding ZIMPOL observation time slots. This shows that the atmosphere was particularly concentrated into the first km, which does not produce significant anisoplanatism. This latter is mostly generated by jet streams between 8 and 12 km, the strength of which has decreased slightly across time.

We report in Table 2 the r_0, average altitude and isoplanatic angle values obtained from the SCIDAR measurements at zenith and $\lambda = 500$ nm. The r_0 value is calculated as follows (Fried 1965):

$$r_0(h > H) = \left(0.423 \left(\frac{2\pi}{\lambda}\right)^2 \int_H^\infty C_n^2(h)\,\mathrm{d}h\right)^{-3/5}, \quad (16)$$

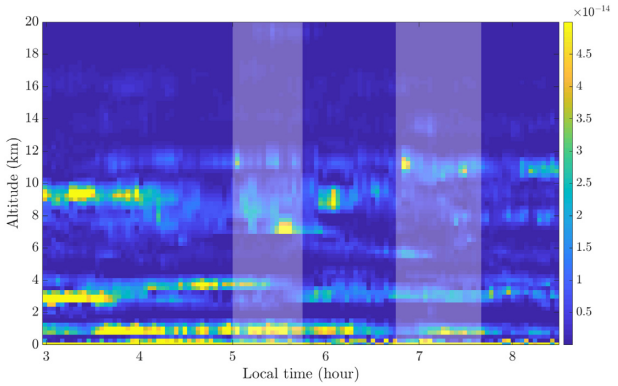

Figure 4. $C_n^2(h)$ estimated by SCIDAR at Paranal (Osborn et al. 2018) across time. White bands correspond to ZIMPOL observing time.

Table 2. Atmospheric characteristics given by the stereo SCIDAR at zenith and 500 nm.

	First slot	Second slot
r_0 (cm)	11.6 ± 1.1	13.8 ± 1.1
$r_0(h>1\,\mathrm{km})$	15.3 ± 1.4	18.5 ± 1.9
$\bar{h}$ (km)	6.4 ± 0.4	6.4 ± 0.8
θ_0 (arcsec)	1.2 ± 0.1	1.4 ± 0.2
θ_0 (line of sight)	1.1 ± 0.1	0.9 ± 0.1

Table 3. PSF FWHMs for the five stars in the field derived from reconstructed PSF models.

	FWHM (mas)
Diffraction @ 554 nm	14
On-axis PSF	33.1 ± 2.0
Off-axis PSF 1	37.4 ± 3.2
Off-axis PSF 2	36.2 ± 2.8
Off-axis PSF 3	38.9 ± 3.9
Off-axis PSF 4	38.6 ± 3.8

where H is the height above which r_0 is measured. The mean-weighted altitude $\bar{h}$ gives the layer height that would produce the same anisoplanatism regarding the C_n^2 distribution and is defined as (Fried 1982)

$$\bar{h} = \left(\frac{\int_0^\infty h^{5/3} C_n^2(h)\,\mathrm{d}h}{\int_0^\infty C_n^2(h)\,\mathrm{d}h} \right)^{3/5}. \quad (17)$$

Finally, the isoplanatic angle that defines the separation angle from the guide star above which the PSF evolves anisoplanatically is calculated from

$$\theta_0 = 0.057\lambda^{6/5} \left(\int_0^\infty h^{5/3} C_n^2(h)\,\mathrm{d}h \right)^{-3/5}. \quad (18)$$

Values in Table 2 show a mitigation of the anisoplanatism effect during the second observing slot, but because of the large telescope zenith angle (60°), the S/N for off-axis star directions has diminished drastically due to (i) atmospheric extinction, which lessens the number of collected photons, and (ii) greater anisoplanatism effects in the telescope line of sight, which decrease the ensquared energy.

Regarding θ_0 and star distance from on-axis, off-axis images should be affected slightly by the anisoplanatism effect. We have measured the PSF full width at half-maximum (FWHM) of five stars as reported in Table 3, which indicates that the AO system did not reach diffraction at 554 nm, which was expected (Fusco et al. 2014). However, separation between the AO correction area and PSF wings is not very clear , advocating that there is an atmospheric or instrumental effect, which looks like a residual jitter according to the elongated PSF pattern, which blurs the image. This is likely introduced by the low frame rate of 300 Hz, which corresponds to the typical coherence time, introducing a large servo-lag error. Consequently, off-axis PSFs are not significantly larger than the on-axis PSF, which suggests that anisoplanatism is there, but the PSF morphology is dominated by servo-lag error.

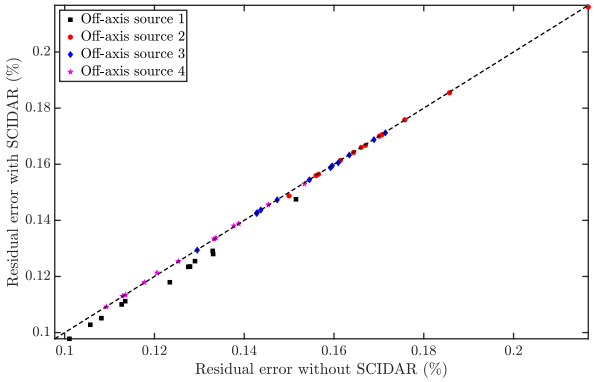

Figure 5. Mean-square error as calculated in equation (22) obtained by best-fitting (stellar parameters only) off-axis sources using an off-axis model (on-axis PRIME + SCIDAR) or the on-axis PRIME PSF. Results were obtained for the first 12 ZIMPOL frames.

Our goal is now to determine whether there is a need to account for anisoplanatism to calibrate the PSF model from off-axis stars. To do so, we have calculated best-fitted off-axis images to retrieve photometry/astrometry using two different PSF models: (i) the on-axis image and (ii) the off-axis PSFs calculated by convolving the on-axis PSF with an anisoplanatism spatial filter calibrated from SCIDAR measurements. If there is real anisoplanatism, the second model should give better results. For S/N reasons, we have treated only the 12 first ZIMPOL frames that were acquired at a lower telescope zenith angle.

In Fig 5, we compare the residual error obtained with equation (22) computed with and without use of SCIDAR data. We see that the off-axis PSF model barely improves the PSF model, but this improvement remains marginal enough to claim that anisoplanatism does not contribute to PSF inhomogeneity, despite star separation being larger than θ_0. We show this in more detail for off-axis star #1 in Fig. 6 : clearly, the residuals do not improve by including the effects of anisoplanatism. This is likely due to a large residual jitter effect in the PSF, which creates an elongated pattern that masks the anisoplanatism feature. In other words, accounting for anisoplanatism produces only a very marginal improvement in the PSF modelling; therefore we chose to consider the PSF as homogeneous across the field, which means that we will derive the PSF from the integrated r_0 value only.

3 PRIME: A COMPLEMENTARY TOOL TO IMPROVE THE CLASSICAL PSF-R SCHEME

3.1 Introduction to PRIME

New approaches must be envisioned to move to the next level of PSF-R. We have introduced the so-called PRIME method (Beltramo-Martin et al. 2019), which yields a built-in parametric

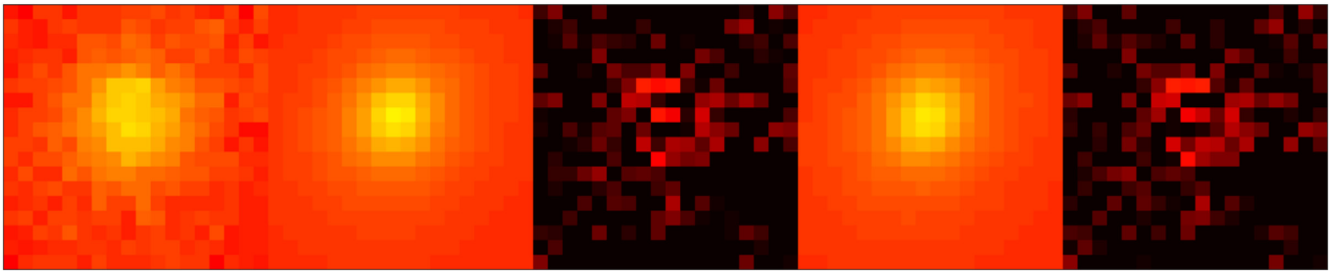

Figure 6. 2D comparison of PSFs using a hyperbolic arcsin scale. From left to right: off-axis star 1 image, on-axis PSF + SCIDAR, corresponding residual, PRIME without SCIDAR, corresponding residual. Reconstructed PSFs were obtained using the 05:04 AO data set.

PSF model using AO measurements. As discussed, the reconstruction usually relies on fudge factors, which are learned by comparing PSF-R with on-sky images and set up as constants afterwards. There have been no attempts so far to figure out whether these fudge factors vary accordingly with observing condition changes. This is what PRIME is going to achieve: it retrieves these factors by adjusting them to match available PSFs in the field. In other words, we combine the pupil plane (PSF-R framework) and focal plane (best-fitting technique) to calibrate the PSF model across fields and spectra. PRIME permits us to avoid collecting specific calibration data for PSF estimation purposes. For instance, there is no more need to offset the telescope or request technical time to test PSF-R. The major drawback is the need for stars in the field, which does not comply with all science cases so far, but we will discuss in Section 3.3 the strategies considered to deliver a PSF regardless of the science field configuration. Assuming that we have stars in the field, PRIME achieves PSF calibration as follows.

(i) **Step 1:** instantiate the PSF model by calculating the covariance matrices introduced in Section 2.

(ii) **Step 2:** extract subfields of an image (user-defined) that contains one or several PSFs.

(iii) **Step 3:** define PSF model parameters to be adjusted. In the following, we will estimate only four parameters, using the following parametrization:

$$\mathcal{B}_\varepsilon(\boldsymbol{\rho}) = r_0^{-5/3} \times (\mathcal{B}_\perp(\boldsymbol{\rho}, r_0 = 1) + g_{\rm al} \times \mathcal{B}_{\rm AL}(\boldsymbol{\rho}, r_0 = 1)) + g_{\rm ao} \times \mathcal{B}_{\rm AO}(\boldsymbol{\rho}) + g_{\rm tt} \times \mathcal{B}_{\rm TT}(\boldsymbol{\rho}), \quad (19)$$

where we assume we work in the isoplanatic regime, e.g. there is no need to include the anisoplanatism covariance function. On top of the r_0 value that will be estimated for the focal-plane image, we include three system parameters $g_{\rm ao}$, $g_{\rm tt}$ and $g_{\rm al}$, which allow us to play with the residual variance level. For a given AO data set, we calculate $\mathcal{B}_{\rm AO}$, $\mathcal{B}_{\rm TT}$ and $\mathcal{B}_{\rm AL}$, while $\mathcal{B}_\perp$ is computed once. In contrast to the model presented in Beltramo-Martin et al. (2019), we have introduced the gain $g_{\rm al}$ to calibrate the aliasing model. The use of $g_{\rm al}$ allows us to account for fluctuations in the wind-speed profile, which enters the computation of the aliasing mode via equation (14) but cannot be determined readily from telemetry data alone.

(iv) **Step 4:** Minimizing a criterion by using a non-linear least-squares minimization algorithm (this is the current implementation, but others may be explored). We have used MATLAB® non-linear problem-fitting facilities based on a trust-region reflective algorithm, as done by Fétick et al. (2019), in order to minimize the following criterion:

$$\mathcal{J}(\boldsymbol{\mu}, \gamma, \boldsymbol{\alpha}) = \sum_{i,j}^{n_{\rm px}} w_{ij} \left[\gamma \times \delta_{\boldsymbol{\alpha}} * h_{ij}(\boldsymbol{\mu}) - d_{ij} + \nu\right]^2, \quad (20)$$

where .∗. is the convolution product and

(a) h_{ij} and d_{ij} are the (i, j) pixel intensity values of the numerical PSF model and sky observation, respectively; the image is converted into e− units using a uniform detector gain of 1.5 e−/ADU (slow pol. mode),

(b) $\boldsymbol{\mu} = [r_0, g_{\rm ao}, g_{\rm tt}, g_{\rm al}]$ is the set of parameters to be adjusted,

(c) $\delta_{\boldsymbol{\alpha}}$ is the Dirac distribution shifted by the astrometric position $\boldsymbol{\alpha}$ and multiplied by the photometric factor γ,

(d) ν is an additional degree of freedom to account for a residual background,

(e) w_{ij} is the weighting coefficient for the (i, j)th pixel.

Identically to what was done by Fétick et al. (2019) and Mugnier, Fusco & Conan (2004), the weighting factor is set to

$$w_{ij} = \frac{1}{\max\{d_{ij}, 0\} + \sigma^2_{\rm RON}}, \quad (21)$$

where $\sigma^2_{\rm RON} = 3$e− for the ZIMPOL detector (slow pol. readout mode: Schmid et al. 2018). The detector noise is assumed to be Gaussian and independent from the data. Also, equation (20) stresses that the model adjustment process retrieves the PSF model parameters (r_0, $g_{\rm ao}$, $g_{\rm tt}$, $g_{\rm al}$) and the stellar parameters ($\gamma, \boldsymbol{\alpha}$) simultaneously. This step automatically outputs the astrometric/photometric measurements of calibration sources.

(v) **Step 5:** Extrapolate the PSF to any desired field and spectrum position.

PRIME offers multiple applications, such as image-assisted error breakdown and photometry and astrometry measurements, as discussed in Beltramo-Martin et al. (2019). In this article, we focus on PSF estimation only. In order to quantify the quality of the PSF fitting, we will evaluate the relative mean-square error, given by

$$\epsilon_h = \frac{\sqrt{\sum_{i,j}^{n_{\rm px}} \left[\widehat{\gamma} \times \delta_{\widehat{\boldsymbol{\alpha}}} * h_{ij}(\widehat{\boldsymbol{\mu}}) - d_{ij} + \widehat{\nu}\right]^2}}{\sum_{i,j}^{n_{\rm px}} d_{ij}}, \quad (22)$$

where $\widehat{\gamma}$, $\widehat{\boldsymbol{\alpha}}$, $\widehat{\boldsymbol{\mu}}$ and $\widehat{\nu}$ are the estimated fitting parameters. The weighting process is particularly helpful to recover all spatial frequencies, without giving more importance to the AO corrected area where pixels are brighter. In particular, this ensures we mitigate biases in the r_0 estimation, which depends significantly on the extended, low-intensity PSF wings. Note that this mean-square error does not include the weight matrix as well as any regularization term we introduce in Section 4. This metric allows us to assess how far the reconstructed PSF, regardless of the approach, is from the on-axis sky image and allows us to analyse different techniques regarding the residual error they lead to.

In the following, we will distinguish between *forward PSF-R*, the reconstruction process that relies on *a priori* parameters (r_0 from

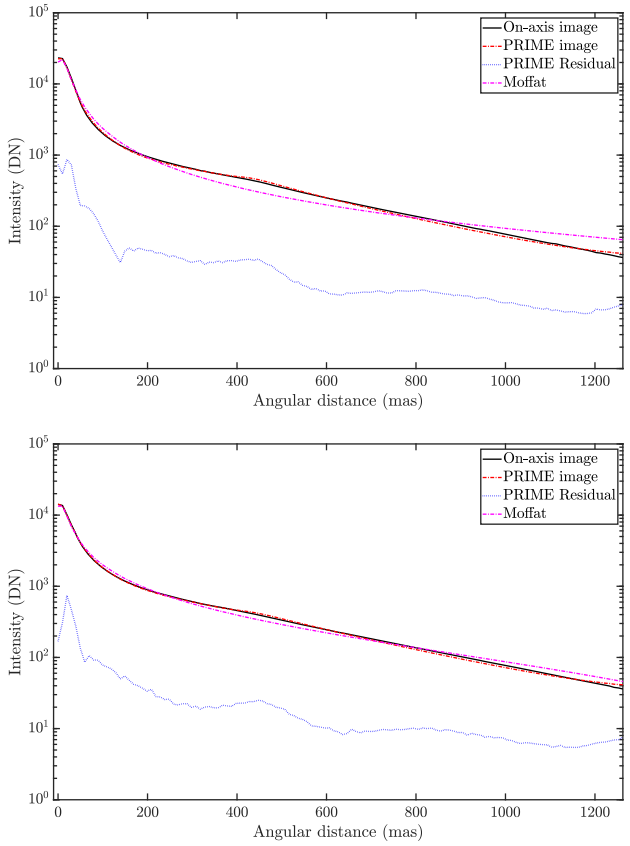

Figure 7. Azimuthal average of sky, PRIME and Moffat-fitted PSFs obtained with (upper) 05:04 and (lower) 06:43 data.

telemetry, $g_{ao} = g_{tt} = g_{al} = 1$), and *PRIME*, the PSF obtained after adjustment over the focal-plane image.

3.2 Maximizing the utmost PSF-R performance

We have tested PRIME by tuning PSF model parameters over a very bright on-axis star, i.e. the star guiding the AO system. The on-axis star is not necessarily present in the field, in particular for laser-assisted systems, so in a way relying on this very bright source is not a nominal situation to deploy PRIME. However, the study of this on-axis star is optimal to test the utmost performance of PRIME, which will seek all possible information on the PSF that is missing in the telemetry data directly in the image itself. On top of that, the very accurate best-fitting parameters found for the on-axis star can then be used as a reference and compared with those (less accurate) found for faint off-axis sources, to assess how PRIME performs in less optimal situations, as we do in Section 4. Finally, in order to provide evidence that PRIME is a good solution for PSF-fitting problems post-AO, we have also herein compared results with a Moffat fitting using the exact same model-fitting process. The Moffat function was defined over seven parameters (Fétick et al. 2019) to allow fitting of an asymmetric PSF shape.

We report in Fig. 7 the comparison between the on-axis PSF profile with PRIME and Moffat fitting as we did with forward PSF-R in Section 2.3.2. Moreover, we present a 2D comparison in Fig. 8 that compares forward PSF-R, PRIME and Moffat fitting and shows at least a factor of 2 improvement on the residual brought by PRIME, especially in the PSF core. The best fit achieves an excellent reproduction of the original image and in both cases,

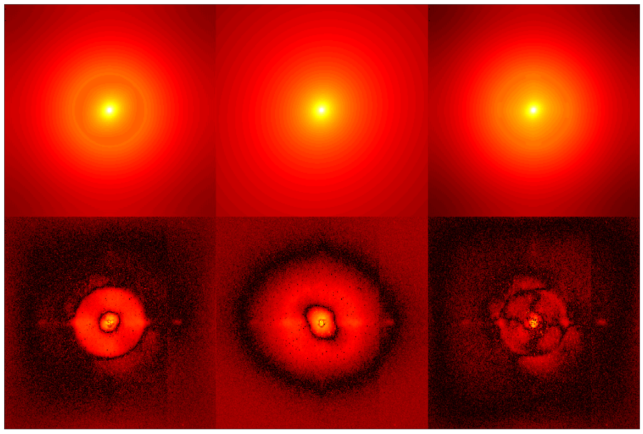

Figure 8. 2D comparison of PSFs (05:03:57) using a hyperbolic arcsin intensity scale. From left to right: forward PSF-R, Moffat-fitting, PRIME. The bottom images are residuals obtained by subtracting the reconstruction to the sky observation.

stressing that the calibration of additional factors on top of the AO telemetry treatment is a must. We also illustrate that the Moffat does not match the on-axis PSF as well as PRIME does, especially due to the PSF structure, which contains an AO-corrected part and seeing-limited wings. We see an improvement of the Moffat fitting in the second case, for which the airmass was larger, however. In this situation, the line-of-sight seeing is worse than previously and the atmospheric residual is large enough to smooth the PSF and attenuate the transition sharpness between the AO corrected and non-corrected areas. However, the Strehl ratio was assessed at 1–2 per cent for these observations and at an imaging wavelength of 554 nm. As a conclusion, even in a very poor correction regime, e.g. when the PSF structure is limited by the atmospheric residual, it is already worth using PRIME instead of an analytical model that is designed to fit seeing-limited images.

3.3 Mitigating required data amount for PSF-R

So far, we have not treated all the ZIMPOL frames we have to hand, only the one that has been acquired synchronously with AO telemetry. A question that appears when talking about PSF-R for the next generation of AO-assisted instruments is related to the amount of data we need to perform PSF-R. In particular, there are some concerns about what is required in terms of storage capability to record all the AO telemetry and associated calibrated matrices systematically. With PRIME, we can address the question: do we necessarily need synchronous AO telemetry with a science frame? To provide hints, we have utilized two AO data sets to reconstruct two different PSF models using either forward PSF-R or PRIME. We end up with four PSF models. With forward PSF-R, the PSF was first reconstructed and then the best fit found (photometry/astrometry) to match the observation. With PRIME, both stellar and PSF parameters were estimated jointly through the model fitting.

We present in Fig. 9 the mean residual error as a function of the estimated r_0 from PRIME and calculated from the residual obtained using forward PSF-R, PRIME or a Moffat model. Several conclusions can be drawn. First of all, PRIME works much better than forward PSF and decreases the residual error by a factor of 3–10 over the 26 frames compared with forward PSF-R, and a factor of 2–4 compared with the Moffat model. Then, forward

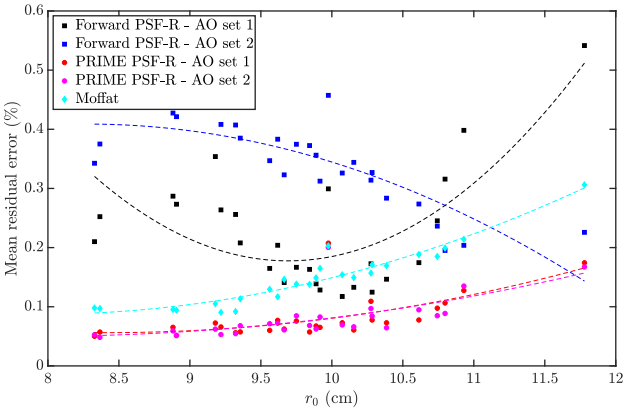

Figure 9. Mean-square error as calculated in equation (22) obtained with both forward PSF-R and PRIME models instantiated with either the 05:04 AO data set (set 1) or the 06:44 set (set 2), as well as the Moffat-fitting results. Dashed lines give quadratic trends with respect to the r_0 estimates obtained with PRIME.

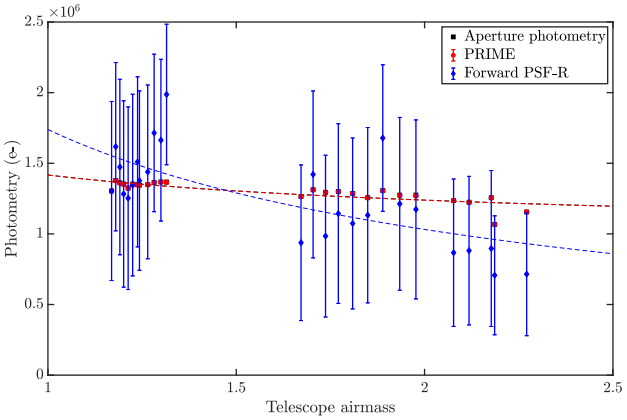

Figure 10. Photometry measurements obtained on the 26 ZIMPOL frames as a function of the telescope airmass. Dashed lines refer to trends in airmass$^{-3/5}$. Error bars are obtained from the fitting minimization function.

PSF-R efficiency degrades significantly when the AO telemetry is not synchronous with the imager frame, especially due to variations of seeing conditions. Finally, PRIME achieves a very stable reconstruction, the residual of which remains pretty much constant, even two hours after having recorded AO telemetry. In other words, temporal variability of atmospheric disturbances can be approximated as a scaling fluctuation of the covariance functions introduced in Section 2. Their structure remains quite similar across time for these specific observations, however.

On top of that, in Fig. 10 we report photometry measurements using either forward PSF-R, PRIME or aperture photometry (sum of pixels). We clearly reveal that PRIME achieves accurate photometry measurements, while forward PSF-R is highly biased and imprecise. This is also indicated by the flux decreasing, due to atmospheric extinction and ensquared energy diminution, which does not decay with a similar slope. Precise assessment of the photometry and astrometry capability of PRIME, with comparison with the standard post-processing pipeline, will be carried out at a later stage.

Furthermore, we have compared r_0 estimates provided by both SPARTA (AO telemetry) and PRIME as a function of SCIDAR measurements, as presented in Fig. 11. As already observed in Fig. 2, we have a large offset between SPARTA and SCIDAR

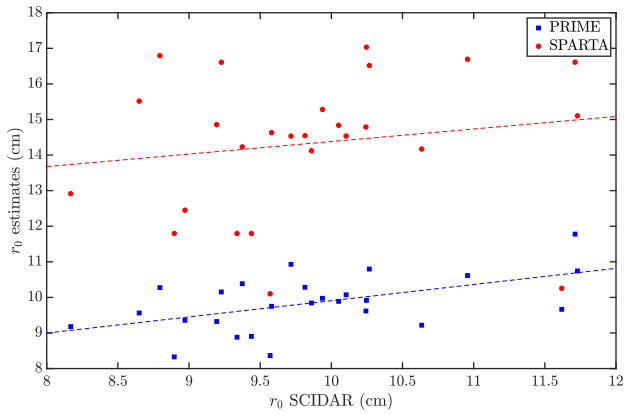

Figure 11. r_0 estimates obtained from SPARTA and PRIME with respect to SCIDAR r_0.

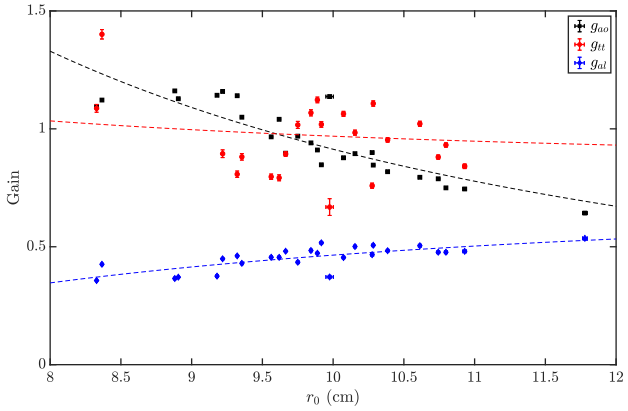

Figure 12. Retrieved values of g_{ao}, g_{tt} and g_{al} as functions of the estimated r_0 value with PRIME. Dashed lines correspond to trends in $r_0^{-5/3}$ using the r_0 estimates from with PRIME.

measurements, which no longer appears when comparing with PRIME results, i.e. PRIME and SCIDAR r_0 estimates seem to comply during this observing night. This also advocates that SPARTA overestimates r_0 by a significant amount, which can be unbiased through calibration using PRIME for as many data as possible.

Finally, in Fig. 12 we present the evolution of retrieved gains with respect to r_0. Identically to what we have done for r_0 estimations, gain values are averaged over results obtained with the two AO data sets, and uncertainties show that they were similar and correlated. Trends with respect to the r_0 estimates from PRIME are obtained using a polynomial fit. These trends allow us to visualize how much the parameters vary with respect to the turbulence strength: they are quite obvious for g_{ao} and g_{al}; when r_0 increases, the turbulence strength and the WFS spot size diminish and consequently the gain value g_{ao} is lessened as well. SPARTA involves a weighted centre-of-gravity algorithm to convert WFS pixels (Petit et al. 2008) into WFS slopes, which may introduce optical gain variations across time as well. Aliasing gain increases slightly with respect to r_0, e.g. for weaker turbulence, which also corresponds to shorter turbulence time (so higher wind speed) according to SPARTA measurements in Fig. 2. As we discussed previously, the aliasing PSD model is effectively sensitive to turbulence velocity variations though modifications of the aliasing transfer function $\mathcal{H}_{\rm cl}$ given in equation (14). This one is derived from the AO closed-loop temporal

Table 4. Final accuracy in Strehl ratio and FWHM obtained with either forward PSF-R (no model adjustment) or PRIME.

	Δ SR (%)		Δ FWHM (mas)	
	bias	std	bias	std
Forward PSF-R slot 1	27	12	4.2	2.1
Forward PSF-R slot 2	12	21	3.5	4.0
PRIME slot 1	0.2	2.9	−0.4	0.9
PRIME slot 2	−0.4	2.2	−0.8	1.6

transfer function (Gendron & Léna 1994), which is converted into a spatial transfer function by turning the temporal frequencies to spatial frequencies using the wind-speed value. Higher wind-speed values tend to introduce more spatial filtering and therefore decrease the aliasing energy. Consequently, PRIME must boost $g_{\rm al}$ in order to match the PSF, as we observe in Fig. 12. Furthermore, $g_{\rm tt}$ seems to vary slightly with respect to r_0 as well, although the trend is not completely clear. We stress that in the V band the Strehl ratio is about 2 per cent and the AO performance is dominated by atmospheric residuals, particularly residual tip–tilt. This latter is influenced by both the seeing and the turbulence velocity, especially for those observations where the system was running at 300 Hz. Fig. 8 illustrates that the PSF is elongated in the 45° direction, certainly due to the combination of the turbulence velocity and AO system servo-lag. In other words, $g_{\rm tt}$ variations must be driven by the temporal properties of atmospheric turbulence as well. More generally, discrepancies around the $r_0^{-5/3}$ trends are trackers to detect $\mathcal{B}_{\rm TT}$ structure changes across time. As we handle the AO telemetry acquired unsynchronously with the imager frame, we compensate for the atmospheric turbulence properties by scaling by a multiplicative factor that applies to those covariance matrices, i.e. we assume that their structures remain identical, only the amplitude changes. PRIME will always retrieve the parameter set that provides the best match with the observed PSF; in other words, these degrees of freedom will absorb any variability of the covariance matrix structure. If we want to use PRIME as a PSF-fitting facility for PSF determination purposes, there is no absolute need to build the PSF model from synchronous telemetry, as PRIME will manage to restore the best PSF model for the observed data set. However, if one cares about the physical meaning of retrieved parameters, we must (i) refine the PSF model as accurately as possible by including all physical effects (static aberrations, cophasing errors, WFS optical gains, etc.) and (ii) confront a PSF model with synchronous observations to mitigate temporal drifts of observing conditions that could be absorbed into the parameter fitting as observed in Fig. 12.

To summarize PSF estimation performance, in Table 4 we report SR and PSF FWHM estimation accuracy. We compare forward PSF-R and PRIME: we highlight that (i) PRIME strongly unbiases estimation of PSF metrics, although some improvement can be pursued in the FWHM, by including the WFS noise model for instance, and (ii) PRIME permits us to reduce the relative error in the SR and FWHM on average by factors of 7 and 2, respectively. Note that the standard deviation is also increased by the quite small amount of data we have, the image noise that contaminates the PSF calibration and the very poor seeing conditions. In this respect, Table 4 provides the best results in a worst-case scenario.

In order to provide more confidence in the retrieval process, we have built an *a posteriori* AO error breakdown to obtain SR values to compare with the image measurements. We estimate the residual error from

$$\sigma_\varepsilon^2 = \sigma_{\rm ao}^2 + \sigma_{\rm tt}^2 + \sigma_\perp^2 + \sigma_{\rm noise}^2, \quad (23)$$

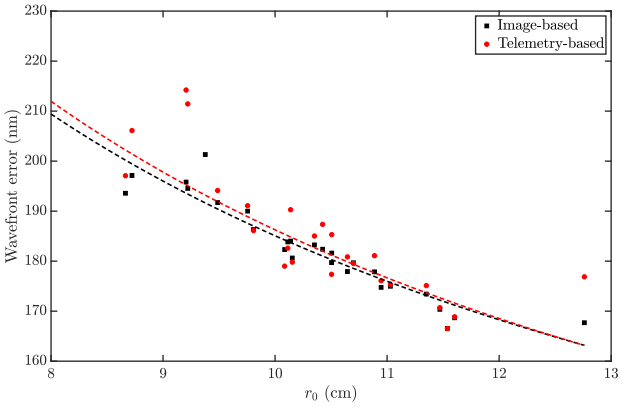

Figure 13. Residual wavefront error with respect to r_0 calculated from either the image SR or the AO telemetry and the PRIME-adjusted parameters. Dashed lines give trends in $r_0^{-5/6}$ using the r_0 estimates from PRIME.

where

(i) $\sigma_{\rm ao} = \sqrt{g_{\rm ao} \times {\rm tr}(\mathcal{C}_{\rm AO})/1377}$ is the tip–tilt excluded AO residual – this is assessed to 135 nm±10 nm over the full observation;
(ii) $\sigma_{\rm tt} = \sqrt{g_{\rm tt} \times {\rm tr}(\mathcal{C}_{\rm TT})}$ – we have retrieved 190 nm ± 18 nm;
(iii) $\sigma_\perp = \sqrt{0.2(d/r_0)^{5/3}}$ is the DM fitting error, which reached 69 nm ± 5 nm;
(iv) $\sigma_{\rm noise}$ is estimated on open loop slopes including tip–tilt and was measured at the level of 46 nm ± 18 nm.

We present in Fig. 13 the residual wavefront error determined from either the SR image or the error breakdown described above. Thanks to PRIME, AO parameters estimates are constrained by the AO telemetry and the PSF morphology as well. On top of the PSF fitting, this gives more evidence that parameters found by PRIME are connected to the system performance.

PRIME offers a new opportunity: instead of acquiring synchronous AO control-loop data with science observations, one may record AO telemetry from time to time, for a sufficient time to make atmosphere characteristics converge, probably at least 30 s (Martin et al. 2012). However, this requires we investigate a few questions, which are as follows. (i) How frequently should we acquire AO data, in other words how frequently does covariance function structure change? (ii) Can we find proper descriptors (seeing, turbulence velocity, telescope elevation) to track structure changes? (iii) Can we enable accurate forward PSF-R by inferring what should be $g_{\rm ao}$, $g_{\rm tt}$, $g_{\rm al}$ and r_0 from contextual data (AO telemetry, external $C_n^2(h)$ profilers, telescope data)? Providing insights into these questions will be the next step of this work.

4 APPLICATION TO FAINT STARS

So far, we have deployed PRIME on the on-axis bright star, with very good conditions of S/N and an absence of crowding. However, PRIME can provide accurate PSF in more challenging conditions, where other alternatives are not feasible. In this section we aim to test the PSF model calibration using off-axis stars, which are much fainter ($m_{\rm V}$ = 15–16 mag). One must consequently rely on a PSF-fitting algorithm to recover the PSF morphology and this situation is ideal to test PRIME capabilities in such a scheme. Besides this, we have highlighted in Section 2.3.3 that the PSF is shift-invariant across the field. In other words, the ground truth is given by the on-axis PSF; the best performance PRIME can achieve in present images is provided in Section 3.2. Nevertheless, in order to mitigate

the noise propagation in our fitting procedure, we must regularize the criterion presented in Eq. 20. We have followed the strategy presented below.

(i) **Step 1:** PSF model parameters r_0, $g_{\rm ao}$, $g_{\rm tt}$, $g_{\rm al}$ are calibrated using off-axis stars #1 and #2 with different regularization strategies presented in Section 4.1. We eventually obtain a calibrated 2D PSF model.

(ii) **Step 2:** The resulting PSF model is used to retrieve the on-axis star's photometry and astrometry; the final accuracy depends on the PSF fitting performance during step 1. Eventually, we assess a mean-square error using equation (22). Thanks to the results presented in Section 3.2, we analyse how the different regularization strategies affect the PSF fitting residual and PSF parameter identification.

4.1 Regularization

We have tested two different regularization strategies.

(i) **Bounds regularization.** We minimize the criterion presented in equation (20) by limiting the parameter space with strict boundaries, inside which the parameter probability distribution is uniform. Bounds are defined relative to $\boldsymbol{\mu}_0$, the solution we have retrieved in Section 3.2:

$$J_B(\boldsymbol{\mu}, \gamma, \boldsymbol{\alpha}) = \begin{cases} J(\boldsymbol{\mu}, \gamma, \boldsymbol{\alpha}) & \text{if } \|\boldsymbol{\mu} - \boldsymbol{\mu}_0\| \leq \boldsymbol{\sigma}_\mu, \\ +\infty & \text{else,} \end{cases} \tag{24}$$

where the constraint is component-wise, as $\boldsymbol{\mu}$ includes several parameters. Therefore, if bounds are set to 0 (no uncertainty), we retrieve the PSF we obtain in our first scenario in Section 3.2, where we use the central star to adjust those parameters. By enlarging bounds around the optimal solution, we make the minimization process more sensitive to the image noise and check how the solution deviates from the optimal one.

(ii) **Gaussian regularization.** We assume that PSF parameters follow a Gaussian distribution $\mathcal{N}(\boldsymbol{\mu}_0, \boldsymbol{\sigma}_\mu)$, where $\boldsymbol{\mu}_0$ is the prior on parameters and $\boldsymbol{\sigma}_\mu^2$ the distribution variance. In order to regularize the problem, we update the criterion given in equation (20) by adding a regularization term to the PSF parameters as follows:

$$\mathcal{J}_{\rm G}(\boldsymbol{\mu}, \gamma, \boldsymbol{\alpha}) = \mathcal{J}(\boldsymbol{\mu}, \gamma, \boldsymbol{\alpha}) + \Gamma \sum_{i=1}^{n_\mu} \left\| \frac{\boldsymbol{\mu} - \boldsymbol{\mu}_0}{\boldsymbol{\sigma}_\mu} \right\|^2, \tag{25}$$

where n_μ is the number of adjusted PSF parameters (we have $n_\mu = 4$ in the present analysis) and Γ a scalar factor that weights the contribution of the regularization term. The present formulation is convenient to separate the parameter precision $\boldsymbol{\sigma}_\mu$, which is identified from calibration (optical gains) of an estimation process (r_0), from Γ, which is a user-defined factor that reflects how much we are confident in $\boldsymbol{\mu}_0$ *a priori* by balancing the weight between the data-based and regularization terms. For instance, if one applies PRIME over successive frames, $\boldsymbol{\sigma}_\mu$ will be delivered for each processed frame as a confidence interval on retrieved parameters that depends on the sole frame only. Thus, we obtain a new $\boldsymbol{\mu}_0$ vector for the next frame and, depending how correlated those two frames are, the user may decide to give more weight to the regularization (boost Γ) or not. Potentially, we can have very precise model-fitting, but the parameters found will not necessarily represent the PSF when treating another frame acquired a few minutes later due to observing condition variations. On the contrary, we could also have badly imprecise estimates due to poor S/N conditions, but stationarity of the observing conditions. Having both parameters $\boldsymbol{\sigma}_\mu$ and Γ allows us to discriminate between PSF parameter precision and accuracy.

However, one must understand that, regardless of the regularization, we are going to bias the PSF fitting results by forcing the solution space to stick around $\boldsymbol{\mu}_0$. The bounds regularization means that the parameter probability density function (pdf) is a gate function and is relevant when we have physical constraints to limit the solution space. Thus, we expect this strategy to propagate more noise, i.e. the PSF fitting residual will degrade with respect to the pdf width. On top of that, the pdf is uniform over the space of acceptable solutions, which means that we do not specifically trust or give more weight to the initial set that feeds PRIME for instantiating the first iteration. Gaussian regularization differs on this point: we must have some confidence in the prior meaningfulness to choose such a regularization.

Our purpose is now to identify how PRIME behaves with respect to (i) the regularization strategy, either a uniform pdf over a bounded space or a Gaussian, and (ii) the degrees of freedom of each of those, i.e. $\boldsymbol{\sigma}_\mu$ (both of them) and Γ (Gaussian pdf only).

4.2 PSF fitting results

First, we have tried PRIME without any regularization, which led to an inefficient reconstruction with a mean residual error (equation 22) of 3 per cent, while we obtained about 0.1 per cent in Section 3.2. The r_0 and $g_{\rm al}$ parameter estimates were particularly biased and physically meaningless, which calls for regularization. In order to provide concise and readable results, we have not set each parameter's precision independently of the others. Instead, we have made $\boldsymbol{\sigma}_\mu$ vary from 0–90 per cent, relative to $\boldsymbol{\mu}_0$. Each parameter pdf width will be absolutely different, but will have the same relative width regarding the optimal solution. Eventually, this methodology will permit us to define which overall parameter precision is required to achieve a given accuracy in the PSF. Also, for the Gaussian regularization, we have also tested different values of Γ (0.001 up to 0.1). The prior $\boldsymbol{\mu}_0$ in equation (25) has been set to the optimal solution found from PRIME in the on-axis image in Section 3.2. Therefore, if we choose too large a value for Γ, the criterion in equation (25) will be dominated by the regularization term and the solution will be very close to $\boldsymbol{\mu}_0$, i.e. we must retrieve the residual error we obtained in Section 3.2. In contrast, if Γ is too low, the regularization term has no impact on the solution and we will propagate too much noise in the solution and obtain meaningless results. The point of this analysis is then to identify which range of Γ must be envisioned to improve results compared with the bounds regularization.

We present the residual error in Fig. 14. Residual errors are calculated by comparing the reconstructed PSF (step 2) with the on-axis image using equation (22). As expected, a wider pdf ($\boldsymbol{\sigma}_\mu$ larger) results in more noise propagation and worse PSF fitting results. Using bounds regularization, the residual error grows quite linearly with respect to $\boldsymbol{\sigma}_\mu$ and we may be able to maintain the residual error below 1 per cent by containing parameters within 40 per cent from the ground truth, while Gaussian regularization allows us to control the slope of this degradation. According to Fig. 12, PSF parameters may vary significantly across time, but variations seem to remain within 50 per cent for this night. If AO telemetry is systematically available with synchronous focal-plane images, these variations should be controlled, as the telemetry signal scales directly with the real r_0 values. In other words, the precision we must consider is given by the standard deviation of parameter estimates from the $r_0^{-5/3}$ trends presented in Fig. 12, which is 10–20 per cent, meaning that PRIME is able to maintain

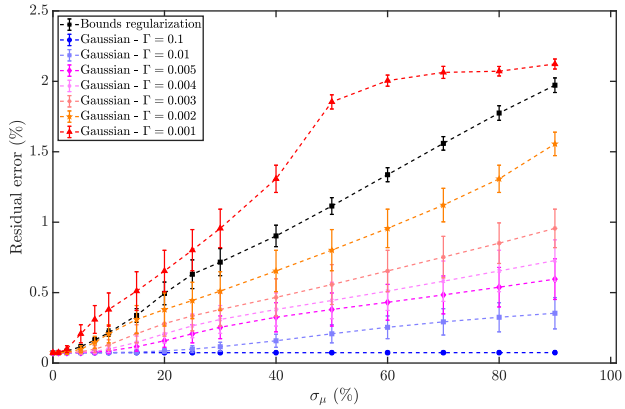

Figure 14. Mean-square error as calculated in equation (22) as a function of $\boldsymbol{\sigma}_\mu$ for several regularization strategies. Errors bars are given by averaging values over the first 12 ZIMPOL frames.

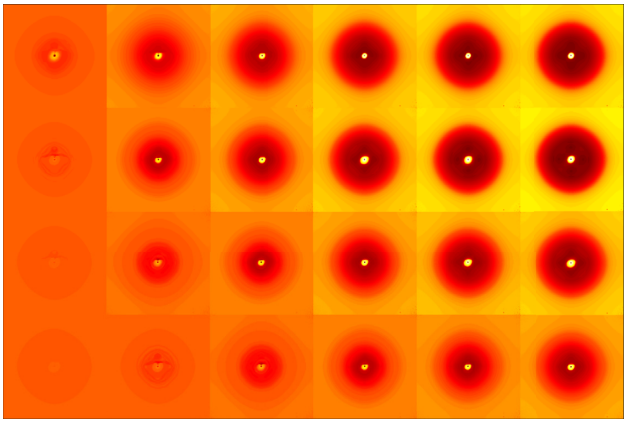

Figure 15. On-axis PSF fitting residual obtained after calibration using off-axis stars and displayed on a hyperbolic arcsin (model underestimation in black) scale. *From left to right:* $\boldsymbol{\sigma}_\mu$ = 1, 5 10, 20, 30 and 40 per cent. *From top to bottom:* bounds regularization, Gaussian regularization with $\Gamma = 0.002$, 0.005 and 0.01.

the mean residual error below 0.5 per cent if synchronous telemetry is provided.

Fig. 15 illustrates how the PSF fitting degrades with respect to $\boldsymbol{\sigma}_\mu$ and Γ. We notice that the inner AO-corrected region is first overestimated for low values of $\boldsymbol{\sigma}_\mu$. For larger values, the residual is mostly dominated by the non-corrected spatial frequencies, with an underestimation of the PSF wings (overestimation of r_0) and an overestimation of the background in equation (20). In other words, adjusted parameters degrade in the opposite direction due to noise confusion, in such a way that the total energy (or flux) is relatively well conserved, while the PSF structure is not.

Figs 16 and 17 present the SR and FWHM estimation error as a function of $\boldsymbol{\sigma}_\mu$ and Γ. We retrieve similar behaviour compared with what we have shown in Fig. 14. The FWHM estimate is getting worse, but remains within 10 per cent as long as the initial guess remains within 40 per cent of the truth. The SR error evolves differently; first it increases and finally it drops down to a negative value: there is a switch that occurs at a $\boldsymbol{\sigma}_\mu$ value that depends on Γ. Below this threshold, noise propagation through the criterion-solving shifts the solution from the ground truth, but without modifying the PSF morphology significantly (the FWHM is reconstructed at a few per cent). Above this threshold value, PRIME

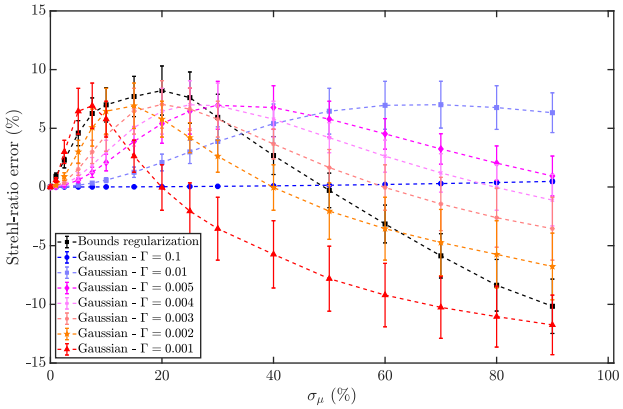

Figure 16. Strehl-ratio error with respect to $\boldsymbol{\sigma}_\mu$ using different regularization strategies.

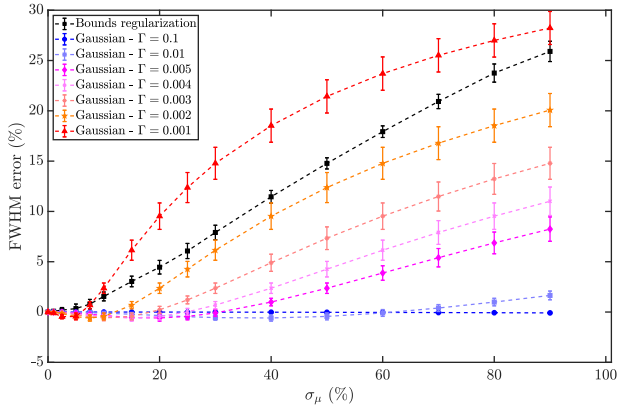

Figure 17. FWHM error with respect to $\boldsymbol{\sigma}_\mu$ using different regularization strategies.

seems to fall into a different local minimum by injecting too much energy into the background and not enough in the PSF wings. However, the SR error stays below 10 per cent despite the PSF structure being badly reconstructed, which advocates exploration of alternative metrics for PSF-fitting quality assessment.

Previous conclusions are confirmed when looking at Fig. 18, which shows the retrieved parameters as a function of $\boldsymbol{\sigma}_\mu$ and regarding several regularization strategies. The bounds regularization shows that $g_{\rm al}$ and $g_{\rm tt}$ degrade linearly with respect to $\boldsymbol{\sigma}_\mu$, while the error on r_0 varies quadratically. This observation reinforces the idea that PRIME confuses the energy between the background and the PSF wings, which speeds up r_0 estimate degradation. In contrast, $g_{\rm ao}$ remains well-estimated to within 10 per cent, as it refers to the AO-corrected area, where the S/N is maximal. This is also reassuring, to confirm that the $g_{\rm ao}$ estimation is decoupled from other PSF parameters.

Regarding PSF fitting and parameter estimation results, we distinguish three different regimes.

(i) $\boldsymbol{\Gamma < 0.002}$: the problem is under-regularized and the fitting residual error increases with respect to $\boldsymbol{\sigma}_\mu$ rapidly up to the worse-case scenario (no regularization). This configuration must be avoided in favour of bounds regularization if $\boldsymbol{\mu}_0$ is not trusted or if we only know physical constraints to bound the solution space.

(ii) $\boldsymbol{0.002 \leq \Gamma < 0.01}$: there is a good balance between data-based and regularization terms and this configuration should be

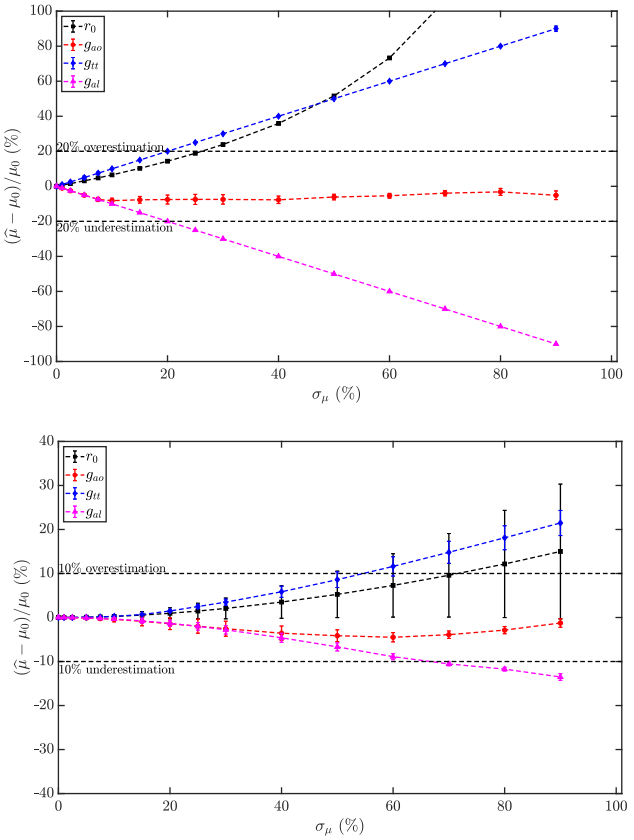

Figure 18. Estimation error in PSF model parameters obtained with PRIME on off-axis stars with respect to $\boldsymbol{\sigma}_\mu$ using different regularization strategies: *Top:* bounds regularization. *Bottom:* Gaussian regularization with $\Gamma = 0.005$.

preferred to the bounds regularization, as long as we have some confidence in the priors $\boldsymbol{\mu}_0$, i.e. we have some evidence that the solution must be close to $\boldsymbol{\mu}_0$. Such confidence can be achieved by processing successive frames or using models of spatial PSF variations to perform the fitting on good S/N PSF first before treating fainter star scenarios.

(iii) $\mathbf{0.01 \leq \Gamma}$: the problem is over-regularized and the adjusted parameters remain very close to $\boldsymbol{\mu}_0$, i.e. the solution is highly biased. This configuration should only serve to update a solution that has been determined over an image highly correlated with the current processed one.

Regarding these results, we may envision performing the PSF fitting with PRIME in a sequential manner: (i) use bright PSFs in the field to constrain the model with bounds regularization and obtain a preliminary set of parameters with associated precision, (ii) redo this process starting from the retrieved parameters as an initial guess and a prior $\boldsymbol{\mu}_0$ with a Gaussian regularization and $\Gamma = 0.002$ and (iii) repeat step (ii) with larger and larger Γ value until reaching the best precision for the parameters. On top of that, we can apply step (ii) to fainter stars to refine the model sequentially using more information without propagating too much noise.

5 CONCLUSION

In this article, we presented an innovative application of the PSF-R method to SPHERE/ZIMPOL data. This is a crucial experiment, since the diffraction limit achieved in the optical with a 10-m class telescope is comparable with ExtremelyLarge Telescopes (ELTs) in the near-infrared. Thus, this kind of study paves the road for exploiting ELTs data reduction.

We have first described how we perform classical PSF-R using SPHERE control-loop data. Unfortunately, the current PSF-R framework does not allow us to achieve proper and stable PSF estimation. In order for improvement, we need to push our AO system understanding deeply through several calibrations, thus demanding a substantial amount of observing and/or technical time.

To overcome this problem, we have introduced the PRIME approach, which is a PSF-fitting technique that inherits from the PSF-R framework to calibrate the PSF model. This is initially instantiated from the AO control-loop data. We have shown that PRIME allows us to achieve very accurate PSF modelling at better than 0.1 per cent of the mean residual, with AO telemetry unsynchronized from scientific images; acquiring 30 s of AO data every hour was sufficient for obtaining excellent results with PRIME.

Finally, we have tested PRIME over faint stars to compare the calibrated PSF with the ground truth given by the on-axis image. This was possible since, as verified using stereo SCIDAR data, anisoplanatism does not contribute significantly to the PSF morphology. In order to enable meaningful PSF estimation in such severe S/N conditions, we have presented two different strategies to regularize the minimization criterion, using either a truncated but uniform pdf or a Gaussian one. PRIME ensures we obtain 1 per cent of mean residual error in the PSF by bounding the solution space within 40 per cent of the optimal solution. Gaussian regularization allows us to increase estimate accuracy up to the optimal achievable performance, depending on how much we trust PSF parameter priors. Gaussian regularization allows the user to adapt the data-based/regularization terms balance in the minimization criterion, depending on how much priors on parameters are trusted. Furthermore, thanks to the PSF-R framework, spatial PSF variations can be modelled accurately, which offers alternative possibilities for PSF-fitting problems: (1) use all external information we have to define PSF parameter priors (stereo SCIDAR for instance); (2) instantiate the PSF model calibration on available PSFs with good S/N and poor crowding using a bounds regularization; (3) use the retrieved information plus variation models to fit the PSF for fainter stars using Gaussian regularization; (4) repeat steps (2) and (3) with updated information on the PSF using Gaussian regularization until reaching the minimal residual.

We plan to push this work further by collecting more science observations, including in a crowded stellar field. When a large sample of data sets is at our disposal, we will apply statistical inference tools in order to capture how PSF model parameters vary with respect to contextual data. This will enable forward PSF estimation in the case of a lack of point sources in the field and enhance PRIME efficiency for stellar field applications.

The next step will be to plug PRIME within a standard image analysis pipeline, in order to combine the strengths of both PSF-R techniques and multi-source image processing tools. This is a necessary step in order to allow high diffusion of the use of PSF-R, which is nowadays confined only to a very few experts.

ACKNOWLEDGEMENTS

The authors acknowledge the French National Research Agency (ANR), who supported this work through the ANR APPLY (grant ANR-19-CE31-0011), coordinated by B. Neichel. GF has been supported by Futuro inRicerca 2013 (grant RBFR13J716).

REFERENCES

Andrade P. P., Garcia P. J. V., Correia C. M., Kolb J., Carvalho M. I., 2019, MNRAS, 483, 1192

Ascenso J., Neichel B., Silva M., Fusco T., Garcia P., 2015, in Don G., ed., Adaptive Optics for Extremely Large Telescopes IV (AO4ELT4), University of California, CA

Beltramo-Martin O., Correia C. M., Mieda E., Neichel B., Fusco T., Witzel G., Lu J. R., Véran J.-P., 2018, MNRAS, 478, 4642

Beltramo-Martin O., Correia C. M., Ragland S., Jolissaint L., Neichel B., Fusco T., Wizinowich P. L., 2019, MNRAS, 487, 5450

Bertin E., Arnouts S., 1996, A&A, 117, 393

Beuzit J. L. et al., 2019, A&A, 631

Britton M. C., 2006, PASP, 118, 885

Butterley T., Sarazin M., Navarrete J., Osborn J., Farley O., Le Louarn M., 2018, in Laird C., Laura S., Schmidt D., eds, Proc. SPIE Conf. Ser., Adaptive Optics VI, Improvements to MASS turbulence profile estimation at Paranal, SPIE, Bellingham, p. 107036G

Ciurlo A. et al., 2018, in Laird C., Laura S., Schmidt D., eds, Proc. SPIE Conf. Ser. Vol. Adaptive Optics VI, SPIE, Bellingham, p. 107031O

Clénet Y., Lidman C., Gendron E., Rousset G., Fusco T., Kornweibel N., Kasper M., Ageorges N., 2008, in Norbert H., Claire M., Peter W., eds, Proc. SPIE Conf. Ser. Vol. Adaptive Optics systems, Tests of the PSF reconstruction algorithm for NACO/VLT, SPIE, Bellingham, p. 701529

Correia C. M., Teixeira J., 2014, J. Opt. Soc. Amer. A, 31, 2763

Diolaiti E., Bendinelli O., Bonaccini D., Close L. M., Currie D. G., Parmeggiani G., 2000, StarFinder: A code for stellar field analysis, Astrophysics Source Code Library, ascl:0011.001

Fedrigo E., Donaldson R., Soenke C., Myers R., Goodsell S., Geng D., Saunter C., Dipper N., 2006, in Brent E., Domenico B., eds, Proc. SPIE Conf. Ser. Vol. Advances in Adaptive Optics II, SPARTA: the ESO standard platform for adaptive optics real time applications, SPIE, Bellingham, p. 627210

Fétick R. J. L. et al., 2019, A&A, 628, A99

Flicker R., 2008, Technical report, PSF reconstruction for Keck AO. W.M. Keck Observatory, Waimea, HI

Flicker R. C., Rigaut F. J., Ellerbroek B. L., 2003, A&A, 400, 1199

Fried D. L., 1965, J. Opt. Soc. Amer. (1917–1983), 55, 1427

Fried D. L., 1982, J. Opt. Soc. Amer. (1917–1983), 72, 52

Fusco T., Conan J.-M., Mugnier L. M., Michau V., Rousset G., 2000, A&A, 142, 149

Fusco T. et al., 2014, in Enrico M., Laird C., Pierre V. J., eds, Proc. SPIE Conf. Ser. Vol. Adaptive Optics Systems IV, Final performance and lesson-learned of SAXO, the VLT-SPHERE extreme AO: from early design to on-sky results, SPIE, Bellingham, p. 91481U

Gendron E., Léna P., 1994, A&A, 291, 337

Gendron E., Léna P., 1995, A&A, 111, 153

Gendron E., Clénet Y., Fusco T., Rousset G., 2006, A&A, 457, 359

Gilles L., Correia C., Véran J.-P., Wang L., Ellerbroek B., 2012, Appl. Opt., 51, 7443

Jolissaint L., 2010, J. Eur. Opt. Soc. – Rapid Publications, 5, 10055

Jolissaint L., Ragland S., Wizinowich P., 2015, in Don G., ed., Adaptive Optics for Extremely Large Telescopes IV (AO4ELT4), University of California, CA, p. E93

Jolissaint L., Ragland S., Christou J., Wizinowich P., 2018, Appl. Opt., 57, 7837

Martin O., Gendron E., Rousset G., Vidal F., 2012, in Laird C., ed., Proc. SPIE Conf. Ser. Vol. Adaptive Optics Systems III, SPIE, Bellingham, p. 84472A

Martin O. A. et al., 2016, Journal of Astronomical Telescopes, Instruments, and Systems, 2, 048001

Masciadri E., Lombardi G., Lascaux F., 2014, MNRAS, 438, 983

Massari D. et al., 2016a, A&A, 586, A51

Massari D. et al., 2016b, A&A, 595, L2

Massari D., Marasco A., Beltramo-Martin O., Milli J., Fiorentino G., Tolstoy E., Kerber F., 2020, preprint (arXiv:2001.08134)

Milli J. et al., 2017, in Maria C., ed., Performance of the extreme-AO instrument VLT/SPHERE and dependence on the atmospheric conditions , Adaptive Optics for Extremely Large Telescopes V, IAC, Spain, preprint (arXiv:1710.05417)

Mugnier L. M., Fusco T., Conan J.-M., 2004, J. Opt. Soc. Amer. A, 21, 1841

Osborn J. et al., 2018, MNRAS, 478, 825

Petit C. et al., 2008, in NorbertH., ClaireM., Peter W., eds, Proc. SPIE Conf. Ser. Vol. Adaptive Optics Systems, SPIE, Bellingham, p. 70151U

Petit C. et al., 2014, in Enrico M.,ed., Proc. SPIE Conf. Ser. Vol. Adaptive Optics Systems IV, SPHERE eXtreme AO control scheme: final performance assessment and on sky validation of the first auto-tuned LQG based operational system, SPIE, Bellingham, p. 91480O

Poyneer L. A., Bauman B., Macintosh B. A., Dillon D., Severson S., 2006, Optics Letters, 31, 293

Ragland S. et al., 2016, in Enrico M., ed., Proc. SPIE Conf. Ser. Vol. Adaptive Optics Systems V, Point spread function determination for Keck adaptive optics, SPIE, Bellingham,p. 99091P

Ragland S. et al., 2018, in Laird C., ed., Proc. SPIE Conf. Ser., Adaptive Optics Systems VI, SPIE, Bellingham, p. 107031J

Rigaut F. J., Véran J.-P., Lai O., 1998, in Bonaccini D., Tyson R. K., eds, Proc. SPIE Conf. Ser., Adaptive Optical System Technologies, SPIE, Bellingham, p. 1038

Roddier F., 1981, Progress in Optics, Vol. 19. North-Holland Publishing Co, Amsterdam, p. 281

Rousset G., Primot J., Fontanella J. C., 1987, LEST Foundation Technical Report, 28, 17

Schmid H. M. et al., 2018, A&A, 619, A9

Schödel R., 2010, A&A, 509, A58

Stetson P. B., 1987, PASP, 99, 191

Tokovinin A., Kornilov V., 2007, MNRAS, 381, 1179

Veran J.-P., Rigaut F., Maitre H., Rouan D., 1997, J. Opt. Soc. Amer. A, 14, 3057

Vigan A. et al., 2019, A&A, 629, A11

Whiteley M. R., Welsh B. M., Roggemann M. C., 1998, Proc. SPIE, 3353, 177

Witzel G. et al., 2016, in Enrico M., ed., Proc. SPIE Conf. Ser. Vol. 9909, The AIROPA software package: milestones for testing general relativity in the strong gravity regime with AO, SPIE, Bellingham, p. 99091O

Yelda S., Lu J. R., Ghez A. M., Clarkson W., Anderson J., Do T., Matthews K., 2010, ApJ, 725, 331

This paper has been typeset from a TEX/LATEX file prepared by the author.